International Journal of Engineering Research & Technology (IJERT)
ISSN: 2278-0181
Vol. 3 Issue 2, February - 2014

Evaporation Assisted CdSe Nanorod Alignment in Microchannels

Kimani A. Stancil

Dept. of Physics and Astronomy
Howard University
Washington,DC, USA

Material Science Division
Lawrence Berkeley Laboratory
Berkeley,CA, USA.

***Abstract*—Evaporation is used to increase the nanorod volume fraction toward a nematic phase to quickly align nanorods on device scales. A statistical assessment of alignment in shallow microchannels is presented using image analysis by polarized microscopy and small angle x-ray scattering. Both 1) solvent annealing, and 2) flow alignment of nanorods is discussed including analysis of intensity weighted orientational order parameters for microscopy and x-ray scattering results.**

Keywords—evaporation; assembly; CdSe nanorods; micro-channel

I. INTRODUCTION

Device scale integration of nanorods continues to advance on micrometer and millimetre scales [1-5]. The nanorod shape enables preferential absorption and emission. And nanorod device integration may eventually mirror current approaches to change the refraction index [6-9]. Special uses of nanorod assembly involve gold nanorods to tune plasmon resonances [9]. Gold nanorods can be locally concentrated by dielectrophoretic methods to form liquid crystal phases from initially dilute dispersions [10-12]. Similarly, we concentrate cadmium selenide (CdSe) nanorods by evaporation to form a liquid crystal phase [13] to effect alignment in devices.

Optically selective and scalable bottom-up devices based on nanorod shape and orientation can be represented by an optical filter with a thin film coating. A thin nanomaterial film may selectively control single or multiple refraction indexes through nanorod material density. In addition to preferential absorption and emission, a nanorod permits the use of two refraction indexes, the extraordinary and ordinary refraction indices, n_e, and n_o respectively. The difference between these indices, $\Delta n = n_e - n_o$ is commonly known as optical birefringence.

Optically birefringent wide-bandgap semiconducting materials, cadmium selenide (CdSe) and cadmium sulphide (CdS), may tailor optical responses in the visible for solid state lighting applications. Their nanorod assembly on substrates provides a small window into potential device assembly [1, 14]. To align nanorods, high weight percent mixtures and monodispersity is desired, however, CdSe nanorods order over long times [13, 15] and synthesis variations produce polydisperse samples. Increases in positional order observed in smectic assemblies result from high monodispersity [4]. Polydisperse samples limit observations of the smectic phase, and they broaden the phase region for isotropic-nematic (I-N) coexistence [16]. This is a practical benefit since device-scale integration using orientational nanorod alignment may proceed without waiting for synthesis techniques to advance.

We apply a combination of phase behaviour and wetting to limit the influence of less controllable factors like turbulence or the range of contact angles accessible to a fluid during evaporation in a microchannel [17]. In this paper, we contribute briefly to the lyotropic phase assisted alignment, wetting, and capillarity as a route to ordering nanorods over large length scales. We offer a revisit to CdSe nanorod assembly by drop-casting dilute solutions and their rapid evaporative and nematic assembly on SU8 microchannels over periods less than 4 minutes with a set completion time of 10 minutes, a timescale used in preparing TEM grids.

In this work, we present a statistical assessment of the resulting nanorod orientation and likely flows in microchannels. Our challenge is met by evaporation where competing solvent and nanoparticle phase transitions combine in a non-equilibrium system to effect changes on large length scales [18]. As the solution color deepens, nanorods concentrate or reorganize with increasing volume fraction shown in Fig. 1. The concentrating effect of evaporation to increase the chance of entering the lyotropic nematic phase is favoured using methylcyclohexane. The solvent is non-volatile and with drop-casting on a flat substrate, evaporation is steady with good nanorod retention until the final drying stages. SU8 coated microchannel surfaces have a water contact angle ~85^o for good wetting by methylcyclohexane. If the channel floors and walls exhibit different contact angles, the asymmetry may set an environment where in the final drying stages, less corner flow may be observed. Corner flow is illustrated in Fig. 1. For our shallow channels (Depth/Width = 0.2 to 0.25 < 1), there is virtually no *dead zone* with respect to transverse capillary pressure and constancy of the radius of curvature. This means that in the limit of low methylcyclohexane or fluid contact angle → 0, that corner flows likely result under pressure driven or shear flow [19]. We then assume that nanorods align with respect to the corner geometry. Fluid pinning is a developed example of contact angle asymmetry that may arise by cross-patterning hydrophobic with hydrophilic regions. For hydrophobic surfaces with hydrophilic nanoscale trenches closely scaled with nanocrystal size, the alignment or confinement of sub-50-*nm* nanocrystals (including tetrapod shapes) has been achieved with evaporation [20, 21]. In this study, we avoid pinning by using SU8 for all channel surfaces, and focus on the collective behaviour of sub-60-*nm* CdSe nanorods resulting from evaporation and capillary effects.

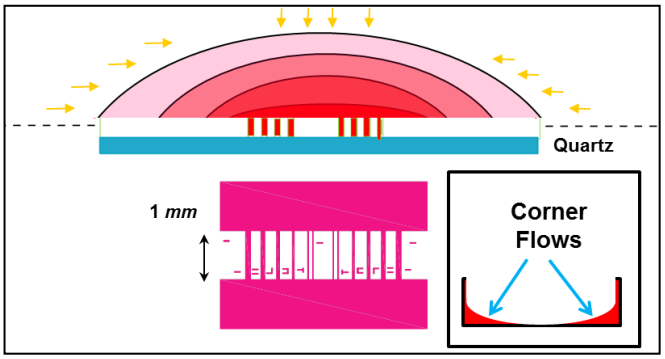

Fig. 1. Drop Casting on a microchannel SU8/Quartz with SU8 floor (5 *um* on quartz) and wall (20 *um*). The solution-substrate-vapor line recedes as solution concentrates. Drying can produce corner flow.

The chances of flow aligning nematics are high under steady flow conditions [22]. Thus, with planar wetting assumed, nanorods are less likely to flow perpendicular to pressure gradients along the channel length. Under nominally ambient conditions in a fume hood, ideal flows may prove elusive and viscous effects become more significant. During evaporation, increases in solution viscosity will diminish the fluid velocity for axial flow [17], thus limiting tumbling or rotation.

To determine nanorod alignment, we apply digital image analysis, and small angle x-ray scattering (SAXS). SAXS confirms a degree of flow alignment that correlates with the channel length. The nanorods flow align with the long-axis parallel to the channel walls for larger aspect ratios (L/D) > 10. And unexpectedly, orthogonal flow alignment occurs for smaller aspect ratio (L/D) < 4, with the short-axis parallel to the channel walls.

II. Experimental

CdSe nanorods are synthesized by known recipe [23] using Tri-octyl Phosphine Oxide (TOPO), Hexyl Phosphonic Acid (HPA), and Tetradecyl Phosphonic Acid (TDPA) ligands and dimethyl cadmium ($CdMe_2$). All precursors were prepared using high purity Argon in a glove box. The nanorod diameter was between 3.7 *nm* and 4 *nm*, with length, L, ranging from 13 *nm* to 57 *nm*.

TABLE I. TEM Statistics (Microchannel)

Aspect Ratio (L/D)	Width (D, nm)	Length (L, nm)
3.6 ± 0.7	3.8 ± 0.7	13.2 ± 1.6
12.4 ± 3.5	3.7 ± 0.7	45.0 ± 11.6
13.1 ± 3.4	4.0 ± 0.7	51.0 ± 10.1
15.6 ± 6.1	4.0 ± 1.3	56.3 ± 9.4

In Table I, we show the TEM statistics for batches in Fig. 2 of which we present SU8 microchannel data with nanorod aspect ratios: L/D = 12.4 ± 3.5; L/D = 13.1 ± 3.4; L/D = 15.6 ± 6.1 ; and a smaller aspect ratio with L/D = 3.6 ± 0.7. In Fig. 2, TEM samples are shown with an instance of an interesting nanorod 'cardinal' or 'nano-bird' assembly for L/D = 13.1 ± 3.4. Initial nanorod dispersions contain anhydrous hexane, and through co-solvent (hexane/2-propanol) cleaning, sedimentation, and centrifugation using the target solvent, methylcyclohexane, sample solutions were prepared at less than 3 *wt. %*. TEM solutions were estimated on the order of 3.2×10^{-4} *wt.%* or less.

A. Preparation of Patterned Substrates.

Quartz wafers (HOYA, 4W 55, 525 *um*) were selected for measuring optical birefringence and small angle x-ray scattering on the same sample. Using photolithography, SU8 (MicroChem 2000 series) coated quartz wafers were prepared for hydrophobic (cured SU8) surfaces. KRUSS contact angle instruments and ASIQ profilometry was used to characterize both surface wetting by water and channel widths and depths. The water contact angle on SU8 was ~ 85°. In Fig. 1, the microchannels are 1 *mm* long. We focus on results for wider channels (80 *um*, and 100 *um*) and the same 20 *um* depths where both SAXS and optical microscopy were easier to measure. For depths less than 20 *um* (i.e. as small as 2 *um*), optical birefringence in the channel was not prevalent. The microchannel design is inspired by a capillarity-driven stop valve to geometrically trap fluid within channels [24]. By creating an abrupt change in the channel width with a transition into a larger reservoir, a pressure barrier forms at the channel ends to stop or limit flow.

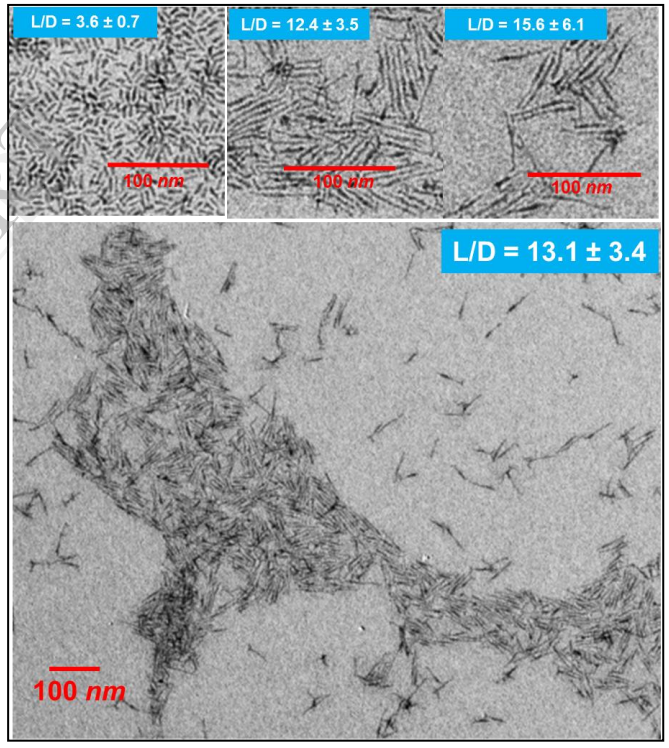

Fig. 2. TEM (Table 1) CdSe nanorods. 'Nano-bird' assembles for L/D = 13.1 ± 3.4.

B. Formation of Dry Assemblies.

CdSe solutions are deposited in a fume hood on a level SU8 patterned substrate shown in Fig. 1. A small volume (0.1*ml*) of CdSe solution is deposited on a 4 *mm* x 3 *mm* multi-channel template with reservoir shown in Fig. 1. During evaporation, the solution-substrate-vapor contact line recedes as material sets inside and outside the channel. SAXS results show larger scattering in channels.

C. Sample Characterization.

All nanorod statistics were obtained using Image Pro software on TEM micrographs established by a Tecnai G2 S-Twin electron microscope (200kV). Polarized micrographs were obtained with a NIKON E600 POL microscope. Digital image analysis using MATLAB estimates relative nematic director orientation based on pixel intensity information.

Equation (1) for intensity, *I*, under crossed polars, determines the orientation angle, β, at a pixel location in the sample plane parallel to the polarizers [25].

$$I = I_o(\sin(2\beta))^2(\sin(\pi d\Delta n/\lambda_o))^2 \qquad (1)$$

The CdSe optical birefringence equals $\Delta n = n_e - n_o = .0197$. The extraordinary index, n_e, is associated with dipoles along the CdSe nanorod's length, and the CdSe nanorod dipole moment scales linearly with nanocrystal volume [26]. The sample, if represented by a single nanorod at each pixel location, produces the orientation angle, β, made with the polarization direction using crossed polars. The intensity, I and I_o, is determined from the greyscale converted image. I_o matches the maximum intensity in a sample image under parallel or 'uncrossed' polarizers. The wave-length equals, λ_o = 532 *nm*, and the sample layer thickness, d = 13.502 *um* corresponding to $(I/I_o) = 1$, when β = .785 radians (45°).

Profilometry measurements (performed at the Howard Nanoscale Fabrication Facility (HNF)) on CdSe nanorod assemblies for unpatterned substrates determine the average sample thickness equalling *z* = 14.8346 ± 4.0955 *um* (measured with *nm* resolution) equivalent to approximately ~3700 nanorods (stacked parallel to the substrate). With digital estimates of a pixel feature density, 379 *pixels/mm* => 2638 *nm/pixel* = *660 nano-rods/pixel*), each β matches on the order of 2,442,000 = 660 * 3700 nanorods.

An assessment of nanorod orientation over select regions of interest (ROI) is based on the digital image content. From histogram information (i.e. number of pixels with the same value of β), an order parameter, *S* (= S_{POL}), in Equation (2a), is computed for each ROI.

$$S = \frac{-2\int_0^{\frac{\pi}{2}} f(\beta)P_2(\beta)\sin(\beta)d\beta}{\int_0^{\frac{\pi}{2}} f(\beta)\sin(\beta)d\beta} \qquad (2a)$$

$$\text{where} \qquad f(\beta) = \frac{N(\beta)I(\beta)}{\sum_{\beta}^{ALL} N(\beta)} \qquad (2b)$$

In equation (2a), $P_2(\beta) = (1/2)*(3\cos^2(\beta) - 1)$, is the 2nd Legendre polynomial for orientational measure. In equation (2b), the function, *f*(β) establishes an intensity weighting based on the histogram information. Each histogram provides the *N*(β), the number of instances where an intensity, *I*(β), occurs. Since at 45° between the polarizer (i.e. the photo's horizontal edge) and analyzer (i.e. the photo's vertical edge), maximal intensity can be obtained for a birefringent sample. There are two different 45° orientations in a channel (i.e. two main diagonals), so that small angle x-ray scattering (SAXS) helps to clarify alignment relative to the channel walls.

Orientational order was confirmed using small angle x-ray scattering (SAXS) with a 100 *um* x 700 *um* beam at the Advanced Light Source (ALS) beamline ALS BL 7.3.3 [27]. Flat-edged quartz wafers and lead tape enabled coincident photolithographic patterning and locating of target samples. As shown in Fig. 3, the substrate is perpendicular to the incident x-ray beam with wave vector, $\boldsymbol{K_I}$. The microchannel lies horizontally, and we use vertical scans to confirm the attenuation of the incident x-rays in a pattern that correlates directly with our 4 mm long template. This is the first evidence of our channels collecting more material in the channel. In Fig. 3, the x-ray scatters from the sample with a final (or scattered) wave vector, KF at an angle ϕ with the incident beam direction.

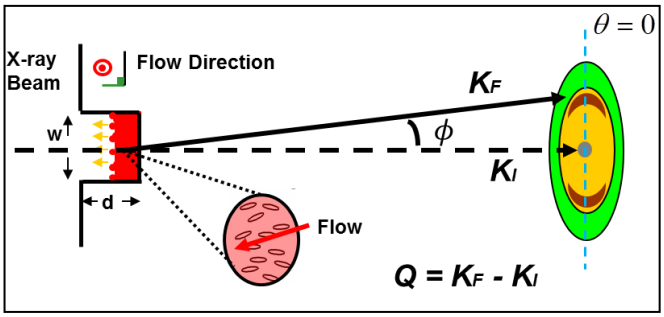

Fig. 3. SAXS geometry. X-ray scatters with scattering vector, $Q = K_F - K_I$. The long axis parallels the channel length when S<0.

The difference in $\boldsymbol{K_F}$, and $\boldsymbol{K_I}$ is called the scattering vector, $\boldsymbol{Q} = \boldsymbol{K_F} - \boldsymbol{K_I}$ with magnitude, $Q = 4\pi \sin(\phi/2)/\lambda$, where λ = 0.124 *nm* is the x-ray wavelength. Peaks in intensity, *I*, reveal structure in *I* vs. *Q* plots. Each SAXS line scan with point scan collection times of 120 seconds are obtained at points separated by 0.25 *mm* over 2 *mm*. Parallel line scans were taken inside and outside a channel. By analysis of scattering from the 2-D Detector image, and through a combination of Igor Pro with NIKA plug-in [28] and Microsoft Excel, an order parameter or alignment factor was computed for different regions of the channel template.

The alignment factor [29], S, in Equation (3) measures orientation at each point along a line scan.

$$S = \frac{-2\int_0^{\frac{\pi}{2}} I_{C,avg}(\theta)P_2(\theta)\sin(\theta)d\theta}{\int_0^{\frac{\pi}{2}} I_{C,avg}(\theta)\sin(\theta)d\theta} \qquad (3)$$

The angle, θ, is the rotation angle in the detector plane (and substrate plane in transmission geometry). $P_2(\theta) = (1/2)*(3\cos^2(\theta) - 1)$, is the 2nd Legendre polynomial. The combination of the azimuthally averaged intensity, $I_{C,avg}$, and $P_2(\theta)$ uncover the mean orientational ordering. The detector's vertical axis (upwards) is aligned with $\theta = 0$. In transmission geometry, we probe nanorod orientation parallel to the substrate. The nanorod's short axis (i.e. width) may align with $\theta = 90°$ and 270°, requiring that the long axis (i.e. length) be vertical with positive values for order (S>0). Alternatively for the transmission SAXS illustration in Fig. 3, the depicted scattering would reflect that the long axis (i.e. length) is horizontal or parallel to the length of a microchannel during a

scan, thus producing negative values of the alignment factor (S < 0).

III. Results and Discussion

CdSe nanorods of the same recipe and similar size as in this study are grown with dipoles along their length [26]. The length is parallel to the extraordinary ray with refraction index, n, and permittivity, $\varepsilon_{\parallel}$, i.e. $n = (\varepsilon_{\parallel})^{1/2}$, and consequently parallel to a liquid crystal (LC) director, $\mathbf{n}_{LC}$, in well-aligned domains. Both the planar sample positioning between crossed polars and the uniaxial nanorod character suggests that optical birefringence correlates well with nanorod orientation [22]. Principle estimates of alignment are based on nanorod orientation that is in the plane of the channel substrate and relatively perpendicular or parallel (i.e. flow alignment) to the channel walls.

The nanorod retaining methycylohexane - CdSe nanorod system enabled a straightforward preparation of dilute solutions with high aspect ratio nanorods. Thus, Onsager's prediction that the onset of isotropic – nematic (I-N) phase coexistence (i.e. aligned nanorods) is easier to observe with dilute solutions of high aspect ratio nanorods (i.e. $\phi_{I\text{-}N} \sim (L/D)^{-1}$) [30]. Inherently, there are two coupled phase transitions, for the solvent and nanorods, so inter-particle interactions must play a significant role in observed order [18]. The uniformity in the observed color changes in solution suggests good blending of CdSe nanorods and methylcyclohexane solvent as the concentration increases.

A. *Polarized Microscopy.*

In practice, optical birefringence is very useful for estimating average domain structure by eye. In this section, sample polarized digital images are presented to make a general assessment of two representative observations: 1) flow alignment resulting from an initial deposition, and 2) flow alignment resulting from solvent annealing. The assessment stems from the determination of the relative orientation angle, β, by use of Equation 1, and concludes with an examination of an orientational order parameter that summarizes the full sampling for multiple regions of interest (ROI) along the channel length. The pictures contain 307, 200 = 640 X 480 pixels, and ROIs contained 225 = 15 X 15 pixels for 80 *um* wide channels; 400 = 20 X 20 pixels for 100 *um* wide channels and for the region between channels.

In Fig. 4, we highlight the optical birefringence and flow alignment from an initial deposition of rods with L/D = 12.4 ± 3.5 (0.1*ml*, 2.96 initial *wt.%*). Images for uncrossed and crossed polarizer images are shown left to right. When the sample is rotated with channels at 45° alignment, the wider 100 *um* channel reveals corner flows with a dark thread along the middle indicated by the blue arrow. Generally, a dark thread would match a liquid crystalline nematic defect, but we conclude otherwise based on the near absence of nanorod material, visible under uncrossed polars. Apparently, flow alignment is significant in both (adjacent) 80 *um* and 100 *um* wide channels.

For each channel, we plot an X-Y map of directors per pixel with orientation angle, β, for each ROI, as shown in Fig. 5 (Left) for the case of solvent annealing. In Fig. 5 (Right), the

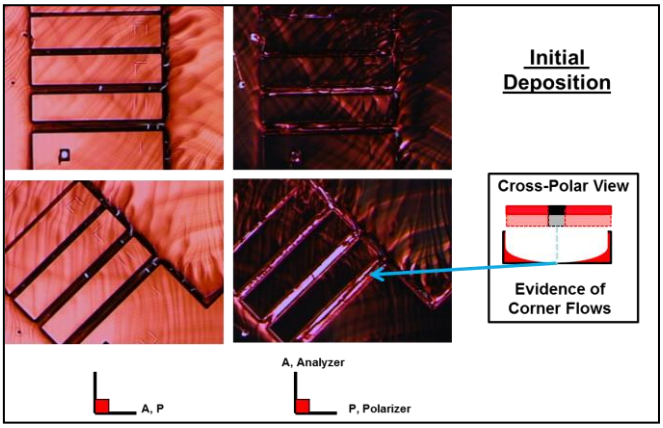

Fig. 4. Image by polarized microscopy. Parallel and crossed polarized images are shown (Left to Right) Rotated sample (Bottom) reveals corner flows with dark thread in 100 *um* channel middle (blue arrow and inset).

histograms contain the number of pixels that have the same orientation angle indicated along the horizontal axis in radian measure (β=.785 radians (45°)). Solvent annealing highlights a general repainting property that results from adding solvent to dry CdSe assemblies. In Fig. 5 (Right - Top insets), nanorods with aspect ratio, (L/D) = 13.1 ± 3.4, show nematic texture but no flow alignment after the initial deposition from a 0.1*ml* of 2.65 *wt.%* solution. However, the same re-dried assembly after 0.16 *ml* of methylcyclohexane was added to increase the time for nanorods to organize in solvent, showed optical birefringence along the channel. Corner flows were partly visible again in 100 *um* wide channels but mainly in regions near the channel ends. In each X-Y map, colored contours highlight pixels with the same orientation angle. In Fig. 5 (Left - Bottom), the contours separate the inside and outside channel.

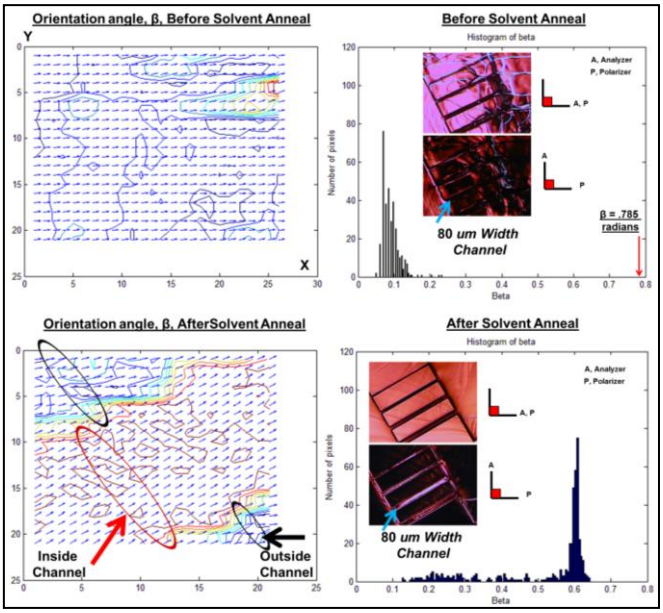

Fig. 5. Director Orientation and Histogram (Left to Right). Top (Initial Dry State); Bottom (Post-anneal). Color contour lines group all pixels with the same orientation angle. Red contour has maximum β values, .6 (or 34.4°).

In Fig. 6, the orientational order parameter, S_{POL}, is determined for nanorods in Figs. 4 and 5. The orientational

parameter S_{POL} results from all ROI information for 80 *um*, 100 *um* channels, and the outside region in between. The better alignment shown by 80 *um* channels is likely due to the observed corner flow in 100 *um* channels. Also, 80 *um* channels are less shallow with slightly higher depth/width ratio. Corner flows may result in the 80 *um* wide channels, but are not easy to detect.

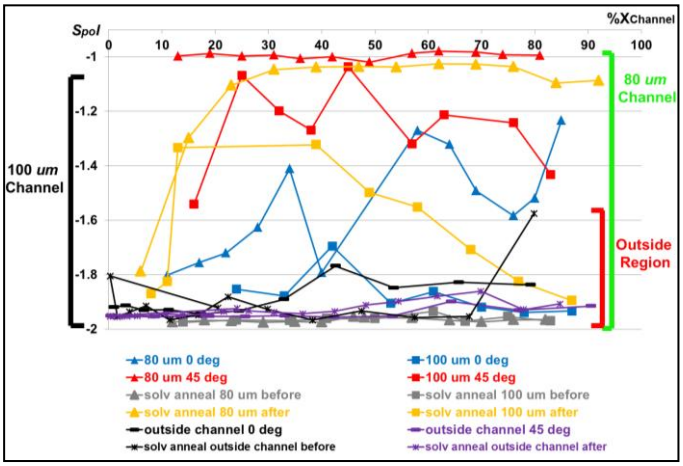

Fig. 6. S_{pol}, vs. $\%X_{Channel}(mm)$. 80 *um*, 100 *um* channels, and outside region are shown.

B. *Small Angle X-ray Scattering (SAXS).*

The assessment of polarized microscopy provides numerical results consistent with the observed optical birefringence. However, the determination of flow alignment is biased by choice of 45° diagonal referenced. SAXS is used to confirm alignment parallel (or perpendicular) to the channel wall. The flow aligning inferences made in the previous section are justified for the high aspect ratio nanorods presented. However, perpendicular alignment does occur with small aspect ratio nanorods. In this section: 1) the method of computing the orientational order parameter, *S*, is explained; 2) parallel alignment and channel length correspondence is demonstrated; 3) nanorod alignment in microchannels is verified using S; and 4) self-assembly on a bare substrate helps to explain the perpendicular channel alignment.

In Fig. 7, the microchannel line scan is linked to the measured I vs. Q plots. SAXS line scans are performed horizontally, parallel to the channel. The analysis present is for line scans including 80 *um* and 100 *um* wide channels and regions in between/or outside. In Fig. 7 (top Right), the average *in-channel* line scans (red curves) indicate a higher scattering intensity than *outside-channel* line scans (green curves). The CdSe nanorod solution is the same shown in Fig. 4 with aspect ratio, (L/D) = 12.4 ± 3.5. Each curve in Fig. 7 (lower Right) matches a different point along the line scan.

Parallel alignment and channel length correspondence is demonstrated in Fig. 8. The azimuthal information is used to compute the orientational order parameter, *S*. In Fig. 8 (top), the azimuthal intensity data selected empirically over a fixed Q-range is obtained from the 2-D detector image using Igor Pro with Nika plug-in [28]. Based on the $I_{azimuthal}$ vs. azimuthal angle, θ, the pixel averaged intensity, $I_{C(avg)}$, is established by a multiple gaussian fit in Fig. 8 (Top). Parallel alignment is indicated since θ = 0° is the vertical reference and the peaks shown are at 0° and 180°.

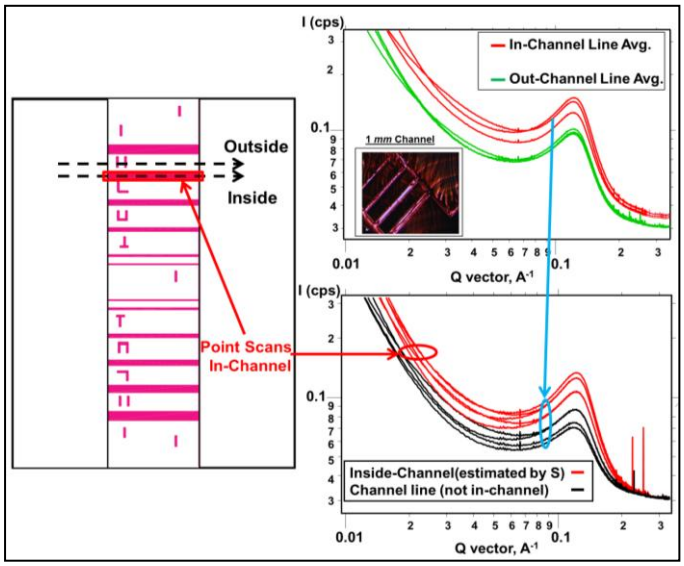

Fig. 7. Microchannel Scans, I vs. Q plot (Left to Right). Template faces beam. A line of point scans along *inside* - and *outside-channels*. (Top Right) I vs. Q, Line Average - *inside* (red)/ *outside* (green); (Lower Right) I vs. Q plot - Point scans (In-Channel, Top)

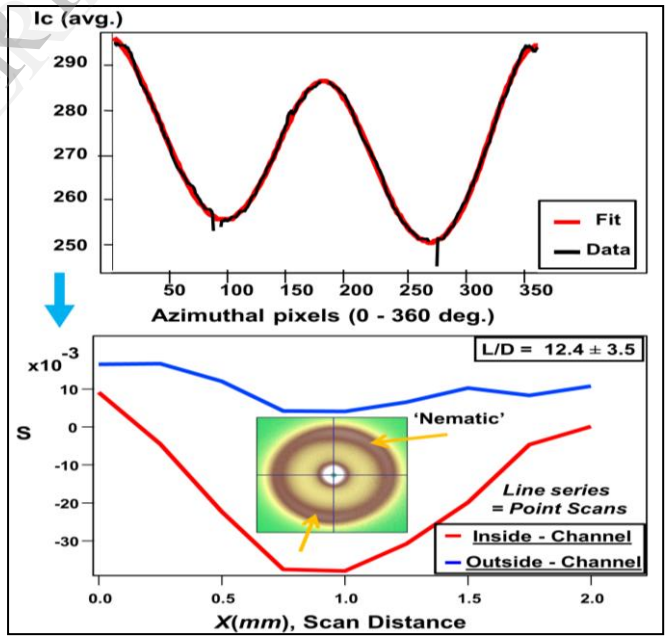

Fig. 8. Azimuthal information and Order Parameter. (Top) I vs. $Q_{azimuthal}$ (Black), Multi-Gaussian Fit (Red); (lower) *S* vs. X(*mm*), in-channel alignment(red) with $S < 0$ range $[0.5\ mm, 1.5\ mm]_X$ match 1*mm* length. Outside channel (Blue).

The order parameter, *S*, calculated in Fig. 8 (lower) highlights each curve in Fig. 7 (lower Right). For the red curve in Fig. 8 (lower), the negative *S* values indicate order along the channel or flow direction. In Fig. 8 (lower inset), we show a 2-D detector image with horizontal nanorod alignment. As a check, we observe ordering in a region $X = 0.5\ mm$ to $1.5\ mm$,

which matches the 1 *mm* microchannel length. The red curves in Fig. 7 (lower Right) are colored red to highlight the channel length correspondence. In addition, the *in-channel* curves show the highest scattered intensity, indicating that our capillary design succeeds in trapping more material in the channel. And the characteristic spacing measured by scattering was approximately ~ 5 *nm* which corresponds to TEM widths equal to 3.7 *nm* ± 0.7 *nm* where the estimated (when considering HPA only) nanorod separation by ligand length equals 1.7 *nm* (or 0.85 *nm* when ligands overlap).

Using evaporation to drive alignment in large aspect ratio nanorods was demonstrated, but unexpectedly, perpendicular alignment indicated by the *S* vs. *X(mm)* graph in Fig. 9 was observed for smaller aspect ratio. In fact, 'crystal-like' ordering or increases in positional ordering occurred since both high Q (width) and low Q (length) SAXS peaks were observed with maximal S-values occurring at the same point, *X*= 1.25 *mm.*

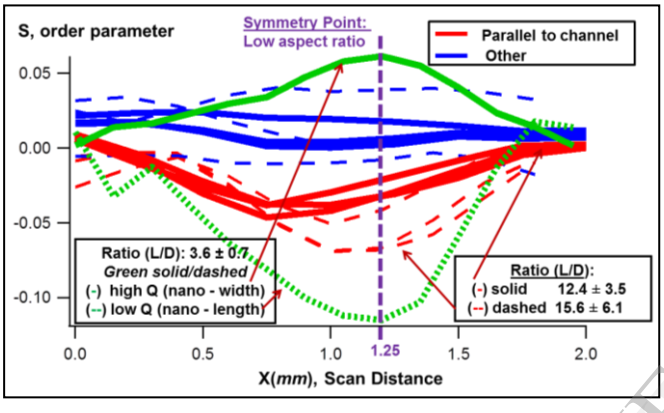

Fig. 9. *S* vs. X(*mm*) - Each *S* value shown is a 4-quadrant average. *Inside* (red)/ *Outside* (blue) channel matches the high Q (width) peak for larger aspect ratio. For small aspect ratio, green solid and dashed curves match high Q and low Q (length) peaks respectively.

Thus, ordering of the long-axis and short-axis is coupled as expected for a single nanorod. The decay away from *X* = 1.25 *mm* in the absolute *S* value along *X*(mm) suggests an absence of material toward the ends of the microchannel which would explain near mirror symmetry demonstrated by the green solid and dashed curves. Fig. 9 includes the scans for high aspect ratio nanorods – L/D = 12.4 ± 3.5, L/D = 15.6 ± 6.1 that show *in-channel* parallel alignment.

When microchannels are not used, circular dry assemblies result on bare substrates. We performed diameter line scans and observe in Fig. 10, *S* vs. %*Xscan* graph, that nanorods mainly order perpendicular to the scan direction.

Alignment parallel to the receding solution-substrate-vapor contact line during evaporation is consistent with minimization of the interfacial free energy at the solution-substrate-vapor interface [31]. The competition between fluid recession during drying and channel wetting may explain our result with small aspect ratio rods in shallow channels. The contact line along the channel floor may recede faster at the channel ends than the volume fraction can increase. To reach the nematic phase sooner, an increase in the initial solution concentration is required as Onsager's theory suggests.

IV. CONCLUSIONS

By examining CdSe nanorod evaporative assembly, we contribute to advancing nano assembly of semiconducting materials. We show that drop-casting dilute nanorod solutions in microchannels can result in compact and aligned nanorods on a millimetre length scale. Our assessment evolves by indirect (polarized microscopy) and direct measure (small angle x-ray scattering) of nanorod assemblies. Microchannels provide orientational and positional ordering and a quick step toward sub-*mm* placement of nanorods. The collective nanorod phase behaviour impacts *nm* to *mm* scale order. Highlighted by 'repainting' or solvent annealing, lyotropic properties may uncover new aspects and control of optically reconfigurable materials.

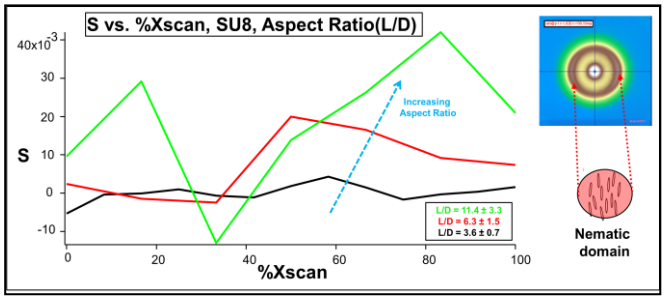

Fig. 10. S vs. %*Xscan* on SU8 (solid). (Bottom -Up) L/D = 3.6 ± 0.7 (black), 6.3 ± 1.5 (red), 11.4 ± 3.3 (green). Assembly orders more with increasing aspect ratio. (Right) Graphical 2-D detector image- Q-space info, i.e. nanorod long axis is *perpendicular to diameter scan*.

ACKNOWLEDGEMENTS

We acknowledge Nicole S. Love for assistance with MATLAB and for helpful discussions on image analysis. Nanorod synthesis, TEM, assembly, and microfabrication (at the UC Berkeley Microfabrication Laboratory) was supported by the Physical Chemistry of Semiconductor Nanocrystals, KC3105, Director, Office of Science, Office of Basic Energy Sciences, of the U.S. Department of Energy (DOE) under contract DEAC02-05CH11231. Author K.A.S. acknowledges A.P. Alivisatos for research support with the Lawrence Postdoctoral Fellowship Program and the Advanced Light Source beamline 7.3.3 that are supported by the same DOE contract. K.A.S. acknowledges A. Hexemer, E. Gann, and E. Schaible (ALS BL 7.3.3) for SAXS support and Howard University (Howard Nanoscale Fabrication facility).

REFERENCES

[1] K. M. Ryan, A. Mastroianni, K. A. Stancil, H. Liu, and A. P. Alivisatos, "Electric-Field-assisted assembly of perpendicularly oriented nanorod superlattices", Nano Letters, 6, 2006, pp. 1479 -1482.

[2] J. L. Baker, A. Widmer-Cooper, M. F. Toney, P. L. Geissler, and A. P. Alivisatos, " Device-Scale Perpendicular Alignment of Colloidal Nanorods", Nano Letters, 10, 2010, pp. 195 -201.

[3] S. Gupta, Q. Zhang, T. Emrick, and T. Russell, "Self-Corralling Nanorods under an Applied Electric Field", Nano Letters, 6, 2006, pp. 2066 - 2069.

[4] C. Querner, M. D. Fischbein, P. A. Heiney, and M. Drndic, "Millimeter-Scale Assembly of CdSe Nanorods into Smectic

Superstructures by Solvent Drying Kinetics", Advanced Materials, 20, 2008, pp. 2308 - 2314.

[5] A. M. Hung, N. A. Konopliv, and J. N. Cha, "Solvent Based Assembly of CdSe Nanorods in Solution", Langmuir, 27, 2011, pp. 12322 - 12328.

[6] G. Mertens, T. Roder, R. Schweins, K. Huber, and H.-S. Kitzerow, "Shift of the photonic band gap in two photonic crystal/liquid crystal composites", Applied Physics Letters, 80, 2002, pp. 1885 - 1887.

[7] D. Erickson, T. Rockwood, T. Emery, A. Scherer, and D. Psaltis, "Nanofluidic tuning of photonic crystal circuits", Proceedings of SPIE Integrated Optics: Devices, Materials, and Technologies XI 2007, 6475, 2007, pp. 647513 - 647523.

[8] T. J. White, A. D. Zhao, S. A. Cazzell, T. J. Bunning, T. Kosa, L. Sukhomlinova, T. J. Smith, and B. Taheri, "Optically reconfigurable color change in chiral nematic liquid crystals based on indolylfulgide chiral dopants", Journal of Materials Chemistry, 22, 2012, pp. 5751 - 5757.

[9] Q. Liu, Y. Cui, D. Gardner, X. Li, S. He, and I. I. Smalyukh, "Self-Alignment of Plasmonic Gold Nanorods in Reconfigurable Anisotropic Fluids for Tunable Bulk Metamaterial Applications", Nano Letters, 10, 2010, pp. 1347 - 1353.

[10] A. B. Golovin, J. Xiang, Y. A. Nastishin, and O. D. Lavrentovich, "Electrically reconfigurable optical metamaterials based on orientationally ordered dispersions of metal nano-rods in dielectric Fluids", Proceedings of SPIE Liquid Crystals XIV 2010, 7775, 2010, pp. 777502.

[11] A. B. Golovin, J. Xiang, Y. A. Nastishin, and O. D. Lavrentovich, "Electro-Optic Effects in Colloidal Dispersion of Metal Nano-Rods in Dielectric Fluid", Materials, 4, 2011, pp. 390 - 416.

[12] A. B. Golovin, and O. D. Lavrentovich, "Electrically reconfigurable optical metamaterial based on colloidal dispersion of metal nanorods in dielectric fluid", Applied Physics Letters, 95, 2009, pp. 254104.

[13] L. S. Li, J. Walda, L. Manna, and A. P. Alivisatos, "Semiconductor Nanorod Liquid Crystals", Nano Letters, 2, 2002, pp. 557 - 560.

[14] L. S. Li, and A. P. Alivisatos, "Semiconductor Nanorod Liquid Crystals and their Assembly on a Substrate", Advanced Materials, 15, 2003, pp. 408 - 411.

[15] L. S. Li, M. Marjanska, G. H. J. Park, A. Pines, and A. P. Alivisatos, "Isotropic liquid crystalline phase diagram of a CdSe nanorod solution", Journal of Chemical Physics, 120, 2004, pp. 1149 - 1152.

[16] M. A. Bates, and D. Frenkel, "Influence of poly- dispersity on the phase behavior of colloidal liquid crystals: A Monte Carlo simulation study", Journal of Chemical Physics, 109, 1998, pp. 6193 - 6199.

[17] R. H. Nilson, S. W. Tchikanda, S.K. Griffiths, and M.J. Martinez, "Steady Evaporating Flow in Rectangular Microchannels", International Journal of Heat and Mass Transfer, 49, 2006, pp. 1603 – 1618.

[18] E. Rabani, D. R. Reichman, P.L. Geissler, and L.E. Brus, "Drying-mediated Self-Assembly of Nanoparticles", Nature, 426, 2003, pp. 271 – 274.

[19] S. W. Tchikanda, R. H. Nilson, and S. K. Griffiths, "Modeling of Pressure and Shear-Driven Flows in Open Rectangular Microchannels", International Journal of Heat and Mass Transfer, 47, 2004, pp. 527 – 538.

[20] Y. Cui, M. T. Bjork, J.A. Liddle, C. Sonnichsen, B. Boussert, and A. P. Alivisatos, "Integration of Colloidal Nanocrystals into Lithographically Patterned Devices.", NanoLetters, 4, 2004, pp. 1093 -1098.

[21] J.A. Liddle, Y. Cui, and A. P. Alivisatos, "Litho-graphically directed self-assembly of nanostructures." Journal of Vacuum Science Technology B", 22, 2004, pp. 3409 - 3414.

[22] Kleman, M., and E. Lavrentovich, *Soft Matter*, Springer-Verlag, 2003.

[23] L. Manna, E. C. Sher, and A. P. Alivisatos, "Synthesis of Soluble and Processable Rod-, Arrow-, Teardrop-, and Tetrapod- Shaped CdSe Nanocrystals", Journal of the American Chemical Society, 122, 2000, pp. 12700 - 12706.

[24] P. F. Man, C. Mastangelo, M. Burns, and D. Burke, "MICROFABRICATED CAPILLARITY-DRIVEN STOP VALVE AND SAMPLE INJECTOR", IEEE The Eleventh Annual International Workshop on Micro Electro Mechanical Systems, 1998, pp. 45 - 50.

[25] R. M. Grechishkin, O.V. Malyshkina, and S. S. Soshin,"Digital Recording and Analysis of Optical-Polarization Images of a Domain Structure", Measurement Techniques, 42, No. 11, 1999, pp. 1043 – 1046.

[26] L.-S. Li, and A. P. Alivisatos, "Origin and Scaling of the Permanent Dipole Moment in CdSe Nanorods", Physical Review Letters, 90, 2003, pp. 097402 - 097405.

[27] A. Hexemer, W. Bras, J. Glossinger, E. Schaible, E. Gann, R. Kirian, A. MacDowell, M. Church, B. Rude, and H. Padmore, "A SAXS/WAXS/GISAXS Beamline with Multilayer Monochromator", XIV International Conference on Small-Angle Scattering (SAS09) IOP Publishing Journal of Physics: Conference Series, 247**,** 2010, 012007

[28] J. Ilavsky, "Nika: software for two dimensional data reduction", Journal of Applied Crystallography, 45, 2012, pp. 324 - 328.

[29] V. M. Ugaz, J. D. K. Cinader, and W. R. Burghardt, "X-ray scattering investigation of highly concentrated poly (benzylglutamate) solutions under shear flow", Journal of Rheology, 42, 1998, pp. 379 - 394.

[30] L. Onsager, "THE EFFECTS OF SHAPE ON THE INTERACTION OF COLLOIDAL PARTICLES", Annals New York Academy of Sciences, 51, 1949, pp. 627 - 659.

[31] J. He, Q. Zhang, S. Gupta, T. Emrick, T.P. Russell, and P. Thiyagarajan, "Drying Droplets: A Window into the Behavior of Nanorods at Interfaces", SMALL, 3, No. 7, 2007, pp. 1214 – 1217.